PNAS RESEARCH ARTICLE | CHEMISTRY

Synergistic dual conversion reactions assisting Pb-S electrochemistry for energy storage

Chiwei Xu[a,1], Zhengwei Yang[a,1], Huihui Yan[a], Jing Li[a], Haoxiang Yu[a], Liyuan Zhang[a], and Jie Shu[a,2]

Edited by Alexis Bell, University of California, Berkeley, CA; received October 11, 2021; accepted January 21, 2022

As one of the most promising cathode materials for next-generation batteries, sulfur has been widely used in organic metal-sulfur batteries, especially in Li-S batteries. However, to date, Pb-S chemistry has never been officially reported. In this paper, a reliable aqueous Pb-S battery based on a dual conversion reaction was constructed. To clarify the feasibility, three important thermodynamic parameters of the Pb-S system were analyzed, including the solubility of PbS in aqueous solution, the volume change of the Pb-S battery system, and the potential of the S/PbS cathode redox couple. Here, it is demonstrated that the aqueous Pb-S battery possesses a great advantage in theory, and the inherent insolubility of PbS makes an aqueous Pb-S system without a shuttle effect. Moreover, the conversion-type counter electrode of a Pb-S system with a stable nucleation rate endows it with a dendrite-free nature, which is quite different from the traditional metal-sulfur battery with a stripping/plating–type counter electrode. Benefitting from these remarkable natures, the aqueous Pb-S battery exhibits a high discharge capacity of 1,343.9 mAh g^{-1}_{sulfur} with a capacity retention of 71.4% after 400 cycles. In addition, the feasibility of this Pb-S system is further demonstrated in a hybrid cell consisting of an S cathode and Zn anode, which affords an energy density of 930.9 Wh kg^{-1}_{sulfur}.

Pb-S chemistry | dual conversion reaction | shuttle effect free | dendrite-free nature | hybrid cell

From the discovery of sulfur-based composite cathode materials in the 1960s to extensive research in sulfur-based carbon encapsulation technology, there is no doubt that metal-sulfur batteries are proving their great research value to the world (1, 2). Among traditional organic metal-sulfur batteries, Li-S batteries in particular possess the greatest commercialization potential due to their high theoretical energy density (2,654.3 Wh kg^{-1}_{sulfur}) (3–5). However, the limitations of the organic electrolyte itself (e.g., low ionic conductivity, flammability, and volatility) (6–8), the shuttle effect of polysulfide, the lithium dendrite, and large-volume changes of the battery system in the process of discharge and charge are all urgent problems to be solved in organic Li-S batteries (9–12). In this case, researchers have begun to focus on high ionic conductivity, nonflammable, and chemically mild aqueous metal-sulfur batteries in recent years (13–20). In these studies of aqueous metal-sulfur batteries, Cu-S, Fe-S, and Zn-S systems have attracted much attention due to their high reversible capacity and excellent cycling performance in aqueous electrolyte. Meanwhile, optimization of the cathode material (14) and electrolyte (17) of aqueous metal-sulfur batteries is also being carried out gradually. However, no new metal-sulfur chemistry was found to undertake the energy storage task, and the exploration of new systems seems to have entered a bottleneck period.

Fortunately, the next system comes into being through our unremitting research. Actually, there are three main thermodynamic conditions existing in the application of metal-sulfur chemistry in an aqueous battery, which are listed as follows: 1) The solubility of metal sulfides (M_xS_y) in aqueous solution; 2) the volume change of the metal-sulfur (M-S) battery system; and 3) the applicability of cathode potential. Here, based on the previous work of our group (12), we further compared Pb-S chemistry with other metal-sulfur chemistry for the above three conditions and found that it has a great advantage in these three conditions. In this paper, we applied Pb-S chemistry to construct an aqueous Pb-S battery consisting of a carbon nanotubes (CNTs)/S composite working electrode, carbon paper counter electrode, and 0.5 M $Pb(NO_3)_2$ electrolyte. For this aqueous Pb-S battery, the reaction on the working electrode is a conversion between S and PbS, and on the counter electrode, it is a conversion between Pb^{2+} and PbO_2. Operating through the synergistic dual conversion reaction, the aqueous Pb-S battery exhibited a discharge capacity of 1,343.9 mAh g^{-1}_{sulfur} in the first cycle and maintained 88% with 1,180.2 mAh g^{-1}_{sulfur} after 140 cycles. Meanwhile, an X-ray diffraction (XRD) study revealed the dual conversion mechanism. Moreover, a prototype $S|Pb(NO_3)_2||Zn|Zn(NO_3)_2$ hybrid cell was constructed, affording an energy density of 930.9 Wh kg^{-1}_{sulfur} at a working voltage of 0.75 V versus Zn^{2+}/Zn.

Significance

Based on the analysis of three thermodynamic parameters of various M-S systems (solubility of metal sulfides [M_xS_y] in aqueous solution, volume change of the metal-sulfur [M-S] battery system, and the potential of S/M_xS_y cathode redox couple), an aqueous Pb-S battery operated by synergistic dual conversion reactions (cathode: $S \rightleftarrows PbS$, anode: $Pb^{2+} \rightleftarrows PbO_2$) has been officially reported. Benefitting from the inherent insolubility of PbS and a conversion-type counter electrode, the aqueous Pb-S battery exhibited two advantages: it is shuttle effect free and has a dendrite-free nature. Moreover, the practical value of the Pb-S battery was further certified by the prototype $S|Pb(NO_3)_2||Zn(NO_3)_2|Zn$ hybrid cell, which afforded an energy density of 930.9 Wh kg^{-1}_{sulfur}.

Author affiliations: [a]School of Materials Science and Chemical Engineering, Ningbo University, Ningbo, 315211, China

Author contributions: J.S. designed research; C.X., Z.Y., and H. Yan performed research; C.X. and J.L. contributed new reagents/analytic tools; C.X., Z.Y., H. Yan, J.L., H. Yu, and L.Z. analyzed data; C.X., Z.Y., and J.S. wrote the paper; and J.S. contributed conceptualization, supervision, funding acquisition, and project administration.

The authors declare no competing interest.

This article is a PNAS Direct Submission.

[1]C.X. and Z.Y. contributed equally to this work.

[2]To whom correspondence may be addressed. Email: shujie@nbu.edu.cn.

This article contains supporting information online at http://www.pnas.org/lookup/suppl/doi:10.1073/pnas.2118675119/-/DCSupplemental.

Published March 14, 2022.

Results and Discussion

Thermodynamic Analysis of Aqueous Pb-S Chemistry. For aqueous metal-sulfur batteries, the solubility of metal sulfide in the electrolyte is seen as a key factor in determining the viability of the battery system. The high solubility of metal sulfide will inevitably cause the shuttle effect, which will further affect the electrochemical performance of the battery. Furthermore, the volume change of the whole battery system in the discharge and charge process is also a prerequisite to evaluate the feasibility of metal-sulfur batteries. Frequent large-volume change not only leads to disconnection of electronic contacts between the active substance and the collector but also causes the active substance to break away from the conductive network built by the conductive agent, making this part of the active substance unusable. In addition, the applicability of the cathode potential is also important and should be considered. For aqueous electrolyte, it possesses a narrow electrochemical stability window (1.229 V) due to the hydrogen and oxygen evolution reactions. On the premise of not adopting "water-in-salt" (21–23), "molecular crowding" (24), "pH-decoupling," and other strategies to broaden the electrochemical stability window of an aqueous electrolyte (25–28), the working voltage of an aqueous metal-sulfur battery should not be higher than 1.229 V, which determines that the cathode potential should not be too high. Meanwhile, under the premise of ensuring a high energy density, the cathode potential also should not be too low. Based on the above three conditions, we compared these parameters of Pb-S chemistry with that of other M-S chemistry (Fig. 1 *A*–*C*; for a detailed calculation process, please refer to the *SI Appendix*). Fig. 1*A* shows the negative logarithm of the solubility product constant (pK_{sp}) of two common hydrolysis routes ($pK_{sp\text{-}a}$ and $pK_{sp\text{-}b}$) of various M_xS_y in aqueous solution. It is not difficult to find that PbS possesses the second-highest $pK_{sp\text{-}a}$ (7.926) and $pK_{sp\text{-}b}$ (28.886), which is slightly lower than the $pK_{sp\text{-}a}$ (8.439) and $pK_{sp\text{-}b}$ (29.399) of InS. It is the low solubility of PbS in an aqueous electrolyte that endows the Pb-S battery with one outstanding property, no shuttle effect. Fig. 1*B* exhibits the volume change rate of various M-S batteries on the basis of total evolution from both the anode and the cathode, and the results show that the Pb-S system presented great advantages compared with other systems. Meanwhile, the S/PbS redox couple also showed a suitable potential value (0.376 V) among these S/M_xS_y redox couples (Fig. 1*C*). Therefore, combined with the above three conditions, it is not difficult to find that Pb-S chemistry has great research value.

At present, with different energy storage behaviors, the counter electrode in a battery can be divided mainly into two categories: a stripping/plating–type counter electrode and a conversion-type counter electrode. Stripping/plating–type

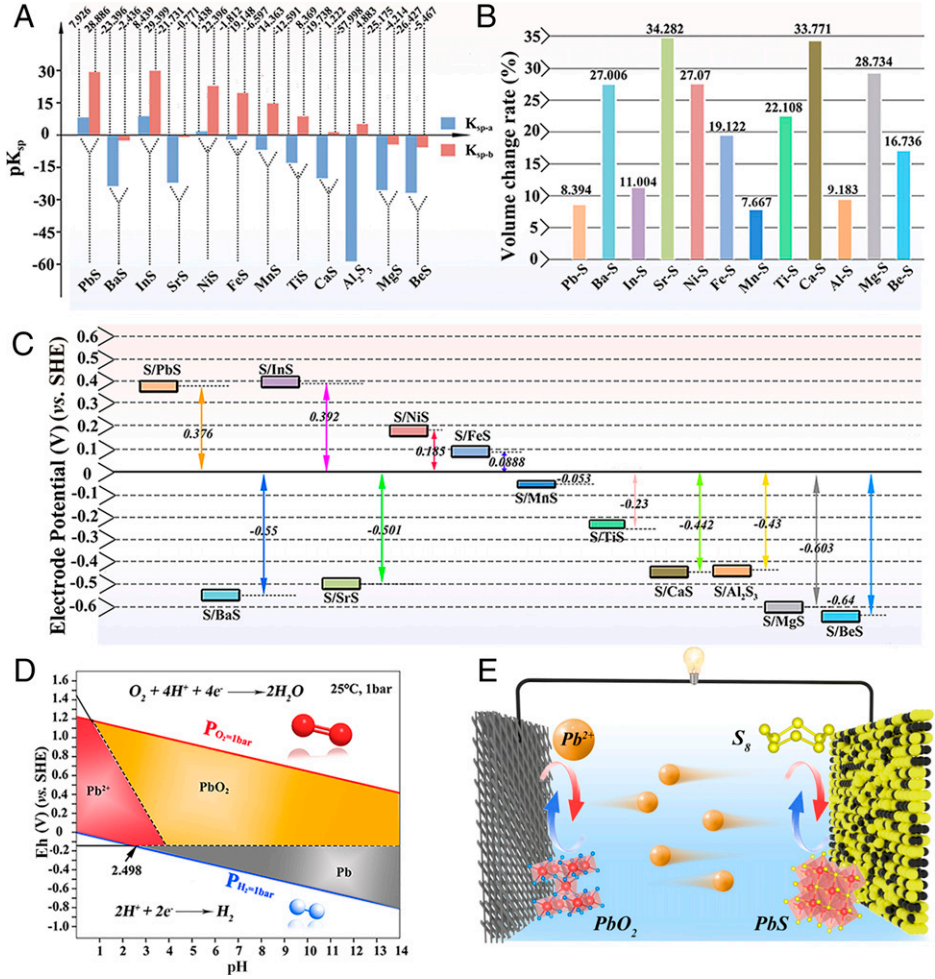

Fig. 1. Thermodynamic analysis of Pb-S chemistry. (*A*) The calculated pK_{sp} values of two common hydrolysis methods of various metal sulfides in aqueous solution. (*B*) The volume change rate of various M-S systems on the basis of total evolution from both anode and cathode. (*C*) The electrode potential versus standard hydrogen electrode (SHE) of various S/M_xS_y redox couples. (*D*) Eh-pH diagrams of 0.5 M $Pb(NO_3)_2$ at 25 °C and 1 atmospheric pressure. (*E*) The working mechanism of the aqueous Pb-S battery. The red and blue arrows represent the discharge and charge reactions respectively.

counter electrodes such as Li (19), Zn (17), and Cu (13) depend on the stripping/plating of metal/metal ions to store energy during the discharge and charge process. It is noteworthy that this type of counter electrode generally has fast reaction kinetics, but the problem of metallic dendrite caused by the uneven charge distribution on the surface of the counter electrode has always been a major challenge. In contrast, conversion-type counter electrodes such as Cd (29), Bi (30, 31), and FeO_x (32, 33), which rely on the conversion of metal/metal oxide or metal oxide/hydroxide for energy storage with a stable nucleation rate, usually do not produce uneven distribution of charge. Fig. 1*D* presents the Eh-pH diagram of 0.5 M Pb^{2+} at 25 °C and 1 atmospheric pressure. For 0.5 M $Pb(NO_3)_2$ solution, the pH value is around 2.4. Hence, it is not difficult to see from Fig. 1*D* that in 0.5 M $Pb(NO_3)_2$ electrolyte, it is a PbO_2/Pb^{2+} redox couple rather than a Pb^{2+}/Pb redox couple that can stably exist in the electrochemical stability window of an aqueous electrolyte. The reaction on the counter electrode in an aqueous Pb-S battery should be based on the conversion reaction between Pb^{2+} and PbO_2 rather than the stripping/plating reaction between Pb and Pb^{2+}. According to a thermodynamic analysis and Eh-pH diagram of $Pb(NO_3)_2$ solution, an aqueous Pb-S battery based on the synergetic dual conversion reaction mechanism (cathode: S ↔ PbS, anode: Pb^{2+} ↔ PbO_2) was first proposed (Fig. 1*E*).

Electrode Conversion Reaction Mechanism. The conversion reaction mechanism of the Pb-S battery was studied in a three-electrode cell consisting of a CNTs/S working electrode, a carbon paper counter electrode, an Ag/AgCl reference electrode, and an 0.5 mol L^{-1} $Pb(NO_3)_2$ aqueous electrolyte. For providing a conductive network to the working electrode, we adopted a melt-diffusion method to infiltrate the insulating elemental sulfur into CNTs (4). Here, the specific surface area of CNTs was about 429.0 m^2 g^{-1} (Brunauer-Emmett-Teller surface area; *SI Appendix*, Fig. S1), which provided a large number of surface-active sites for conversion reaction. *SI Appendix*, Fig. S2 exhibits the scanning electron microscopy (SEM) image of as-prepared CNTs/S nano-composite, and the mass loading of S in the CNTs/S composite was controlled at ∼60 wt % (*SI Appendix*, Fig. S3). It should be noted that 60% sulfur content was intended to facilitate the experiment, but a higher sulfur content is more valuable for practical applications. Moreover, the hydrophilicity test adopted on CNTs/S cathode shows that the water droplet on the cathode surface presented a small contact angle of 69.2° to the horizontal plane, indicating that this composite cathode material possesses a high hydrophilicity (*SI Appendix*, Fig. S4).

The conversion mechanism on the cathode of aqueous metal-sulfur batteries presents a common characteristic. During the discharge process, metal is oxidized to produce metal ions, and electrons are released simultaneously. When electrons reach the cathode via the external circuit from the anode, metal ions have a tendency to travel through metal salt electrolyte toward the cathode; finally, metal sulfide forms at the end of the discharge process. During the charge process, the reaction is reversed, and metal sulfide is eventually converted back to S. In order to prove the formation of PbS in the discharge process (Fig. 2*A*) and its reversible conversion to S in the charge process (Fig. 2*B*) on the cathode of the Pb-S battery, transmission electron microscopy (TEM) measurement was performed to unveil the detailed reaction process. As shown in Fig. 2*C*, TEM elemental mapping images of complete discharge products showed uniform distribution of S and Pb elements on the cathode. In the high-resolution TEM image, the crystal lattice fringe of 3.42 Å corresponded well with the featured (111) plane of PbS, which confirms that PbS is the final product of the cathode discharge reaction. In the complete charge state, only that S element can be observed in the final product, and the interplanar spacing of 3.85 Å also corresponds to the featured (103) facet of S, which confirms that PbS was eventually converted back to S during the charge process (Fig. 2*D*). Furthermore, the dynamic evolution between PbS and S on the cathode during the discharge and charge process from −0.2 to 0.6 V versus Ag/AgCl at 0.5 A g^{-1} is further elucidated by an XRD test (Fig. 2 *E*–*H*). When the CNTs/S cathode started to discharge, eight new peaks at Bragg positions of 30.06°, 43.03°, 50.95°, 53.39°, 62.49°, 68.84°, 70.89°, and 78.88° appeared in Fig. 2 *F*–*H*, which matched well with the featured diffraction peaks of PbS (Joint Committee on Powder Diffraction Standards [JCPDS] No. 65–0692). At a fully discharged state of −0.2 V versus Ag/AgCl, the signal strength of these peaks reached its maximum, which means that S was completely converted to PbS. In the subsequent charge process, the signals of these peaks gradually weakened and completely disappeared at the fully charged state of −0.6 V versus Ag/AgCl, which means that PbS was totally converted into S in the charge process. The detailed XRD patterns of the cathode in the original state, fully discharged state, and fully charged state can be found in *SI Appendix*, Fig. S5. Obviously, when these TEM and XRD results are combined, the cathode reaction mechanism can be summarized by the follow equation:

$$S + 2e^- + Pb^{2+} \underset{\text{charge}}{\overset{\text{discharge}}{\rightleftarrows}} PbS. \quad [1]$$

For the reaction on the anode of the metal-sulfur battery being studied at present (Cu-S, Fe-S, Zn-S, etc.), both depended on the stripping/plating reaction of metal ions. However, according to the Eh-pH diagram analysis of $Pb(NO_3)_2$ solution (Fig. 2*D*), it is the PbO_2/Pb^{2+} redox couple rather than the Pb^{2+}/Pb redox couple that can stably exist in the electrochemical stability window of an aqueous electrolyte. Thus, the reaction on the anode of an aqueous Pb-S battery should be the conversion reaction based on the PbO_2/Pb^{2+} redox couple. For verifying the conversion reaction of PbO_2 during the discharge process (Fig. 3*A*) and the following reduction behavior to Pb^{2+} during the charge process (Fig. 3*B*), the SEM was performed on the final product of the anode in the complete discharge and charge states. As expected, in the complete discharge state, PbO_2 was deposited in the form of "pomegranate" on carbon fibers without other impurities, and the elemental mapping images of O and Pb further testify to this viewpoint (Fig. 3*C*). In the complete charge state, PbO_2 was almost dissolved back to the electrolyte, and the attenuation of the O and Pb elemental signal in mapping images is also consistent with this phenomenon (Fig. 3*D*). For further validation, SEM images of PbO_2 with different resolutions in the discharge and charge states are exhibited in *SI Appendix*, Fig. S6. It can be seen that PbO_2 is precisely distributed on the carbon fiber with pomegranate morphology without obvious spikes, which largely reflects the dendrite-free characteristic of this aqueous Pb-S battery. In addition, the XRD investigation further revealed the mechanism behind the conversion of PbO_2 and Pb^{2+} during the discharge and charge process. When PbS began to decompose on the cathode, PbO_2 also began to deposit on the anode. It can be seen in Fig. 3 *E*–*H* that characteristic peaks such as (110), (111), (002), (020), (200), (021), (130), (132), and (221) reflections of PbO_2 (JCPDS No.45–1416) began to

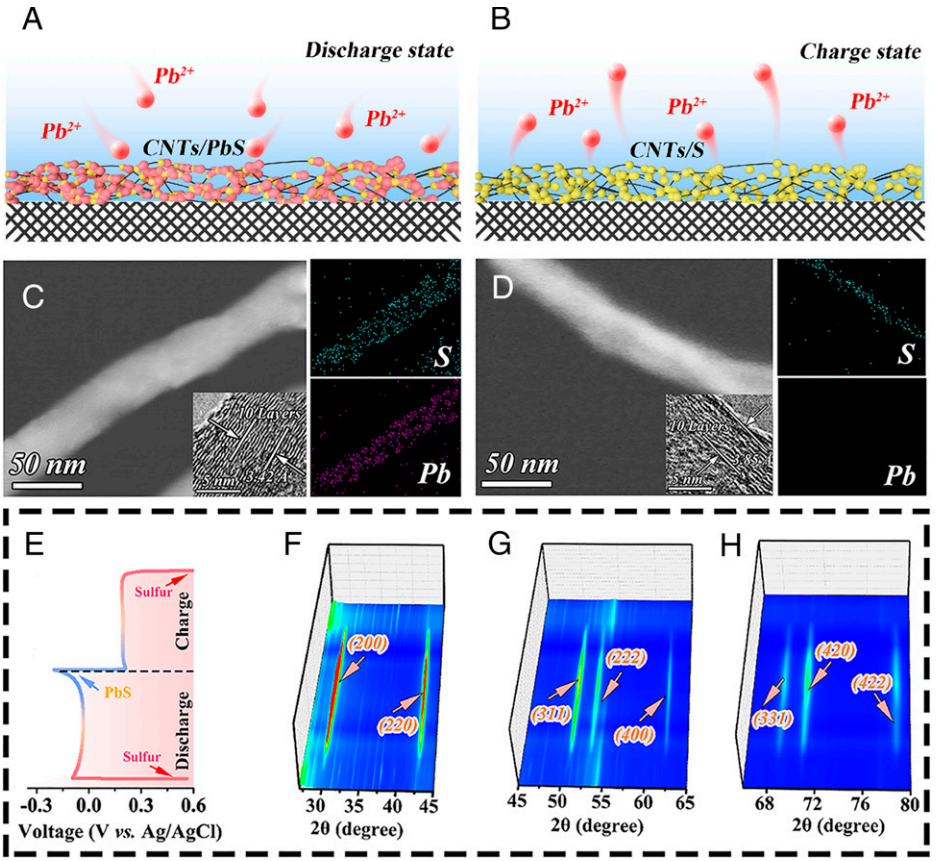

Fig. 2. Cathode conversion reaction mechanism. (*A*) Schematic illustration of the formation of PbS on the cathode in the discharge process. (*B*) Schematic illustration of the formation of S on the cathode in the charge process. (*C*) TEM image of the CNTs/S cathode and corresponding element mappings of S and Pb in the discharge state. The inset displays the lattice spacing of (111) plane of PbS. (*D*) TEM image of the CNTs/S cathode and corresponding element mappings of S and Pb in the charge state. The inset displays the lattice spacing of (103) plane of S. (*E*) GCD profiles of the aqueous Pb-S battery at 0.5 A g^{-1}. (*F*) XRD patterns collected on the cathode in the first cycle within the 2-theta range of 27°to 45°. (*G*) XRD patterns collected on the cathode in the first cycle in the 2-theta range of 45° to 65°. (*H*) XRD patterns collected on the cathode in the first cycle in the 2-theta range of 66° to 80°.

appear gradually along with the discharge reaction and reached maximum intensity at the complete discharge state. As the charge reaction went on, the relative intensity of these peaks began to decrease and completely disappeared in the complete charge state, which means that the PbO_2 was stripped off the anode. The detailed phase structures of the anode in the original state, fully discharged state, and fully charged state can be further demonstrated by the XRD patterns in *SI Appendix*, Fig. S7. In conclusion, through these SEM and XRD results, the anode reaction mechanism can be summarized by the follow equation:

$$Pb^{2+} + 2H_2O - 2e^- \underset{\text{charge}}{\overset{\text{discharge}}{\rightleftarrows}} PbO_2 + 4H^+. \qquad [2]$$

Electrochemical Performance of Aqueous Pb-S Battery. Operating by the synergistic dual conversation mechanism of cathode and anode, the aqueous Pb-S battery showed excellent electrochemical performance. For distinguishing the charge-discharge platforms, we first studied the cyclic voltammetry (CV) curve under a scan rate of 0.5 mV s^{-1} (Fig. 4*A*). The results indicate that the reversible energy storage source mainly comprised one reduction peak at ∼0 V versus Ag/AgCl, and one oxidation peak at ∼0.12 V versus Ag/AgCl. Fig. 4*B* shows the galvanostatic charge/discharge (GCD) profiles collected at 0.5 A g^{-1}. Notably, the Pb-S battery delivered an initial discharge capacity of 1,343.9 mAh g^{-1}_{sulfur} and maintained a reversible capacity of 1,267.5 mAh g^{-1}_{sulfur} in the following cycles. In addition, Fig. 4*C* compares the polarization value between this Pb-S battery and other aqueous metal-sulfur batteries, in which the aqueous Pb-S battery showed relatively lower polarization (0.35 V) than that of aqueous Ni-S (0.4 V), Zn-S (0.9 V), and Co-S (1.0 V) systems (13). Meanwhile, electrochemical impedance spectroscopy analyses demonstrated that the charge transfer resistance of the Pb-S battery was 3.1 Ω before the initial cycle and 4.2 Ω after 60 cycles (*SI Appendix*, Fig. S8), which proves that the Pb-S battery possesses fast and stable reaction kinetics. Benefiting from this superiority in electrochemical kinetics, the Pb-S battery showed outstanding rate capability, where the discharge capacity was 1,498; 1,463; 1,397; 1,343; and 1,180 mAh g^{-1}_{sulfur} at 0.2, 0.3, 0.4, 0.5, and 0.8 A g^{-1}, respectively (Fig. 4*D*). In addition, X-ray photoelectron spectroscopy study of the postcycle anode showed that there was no Pb-S bond at the discharge state (*SI Appendix*, Fig. S9); hence, the shuttle effect was nonexistent. Meanwhile, the entire structures of the cathode before and after 60 cycles were analyzed via SEM (*SI Appendix*, Figs. S10 and S11). Obviously, there was no structural collapse on the cathode after 60 cycles. Therefore, benefiting from the dissolution-free, dendrite-free nature and structural stability, the Pb-S battery exhibited good cycling stability (Fig. 4*E*). After 140 cycles at 0.5 A g^{-1}, the aqueous Pb-S battery still exhibited a reversible capacity of 1,180.2 mAh g^{-1}_{sulfur} with a capacity retention of 88%. It is worth noting that the precipitous decline of capacity that existed in this Pb-S battery after 140

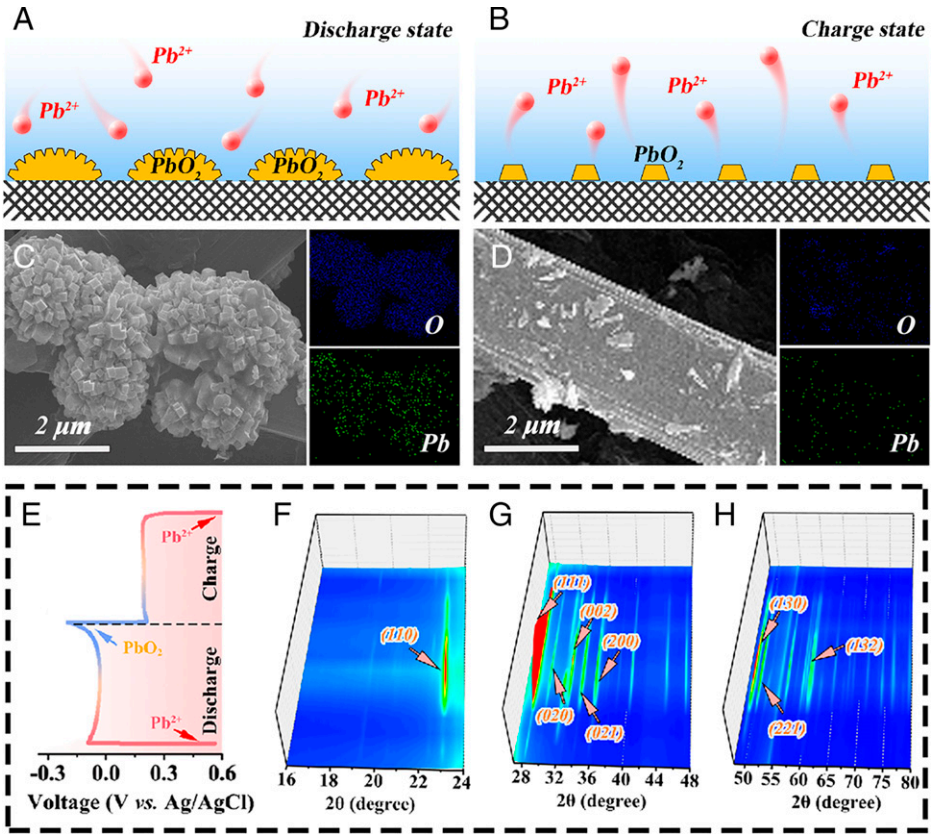

Fig. 3. Anode conversion reaction mechanism. (*A*) Schematic illustration of the formation of PbO_2 on the anode in the discharge process. (*B*) Schematic illustration of the dissolution of PbO_2 on the anode in the charge process. (*C*) SEM image of the complete discharge product on the anode and corresponding element mappings of O and Pb. (*D*) SEM image of complete charge product on the anode and corresponding element mappings of O and Pb. (*E*) GCD profiles of the aqueous Pb-S battery at 0.5 A g^{-1}. (*F*) XRD patterns collected on the anode in the first cycle in the 2-theta range of 16° to 24°. (*G*) XRD patterns collected on the anode in the first cycle in the 2-theta range of 27° to 48°. (*H*) XRD patterns collected on the anode in the first cycle in the 2-theta range of 48° to 80°.

cycles could be almost eliminated after replacing the anode. We speculate that this may be related to the residual PbO_2 in the charge state on the anode, which highlights the challenge of the anode on the reversibility of the aqueous Pb-S battery. With a refreshed anode, this Pb-S battery maintained a high-capacity retention of 71.4% after 400 cycles, delivering a reversible capacity of 960 mAh g^{-1}_{sulfur}. Furthermore, the cycling performance was also tested at a lower current density (0.3 A g^{-1}). The result revealed that the discharge capacity was retained around 95% with 1,390 mAh g^{-1} after 60 cycles, and the polarization of the Pb-S battery stably remained at a low value (around 0.3 V) under different cycles (*SI Appendix*, Fig. S12). In order to present a more intuitive understanding of the cycle performance of Pb-S system, we compared the electrochemical performance of the Pb-S battery with that of other metal-sulfur systems. The results show that Pb-S had a high specific capacity and excellent cyclic stability (*SI Appendix*, Fig. S13).

Although the Pb-S battery exhibited excellent cycle and rate performance, the low output voltage limits its practical application. To address this problem, we designed a $S|Pb(NO_3)_2||Zn(NO_3)_2|Zn$ hybrid cell using an anion exchange membrane to divide the cell into two compartments: a CNTs/S cathode and a zinc metal anode. Fig. 4*F* exhibits the operation mechanism of this hybrid cell. During the discharge process, S obtained two electrons and combined with Pb^{2+} to form PbS, while Zn metal was oxidized into Zn^{2+}. During the charge process, the reaction was in the opposite direction. For balancing the charge neutrality, $[NO_3]^{2-}$ acted as commuting shuttles between $Pb(NO_3)_2$ and $Zn(NO_3)_2$ electrolytes in the two compartments. The reactions in the discharge process can be expressed as follows:

$$\text{Cathode}: \quad S + Pb^{2+} + 2e^- \rightarrow PbS, \qquad [3]$$

$$\text{Anode}: \quad Zn \rightarrow Zn^{2+} + 2e^-, \qquad [4]$$

$$\text{Full cell}: \quad S + Pb^{2+} + Zn \rightarrow PbS + Zn^{2+} + 2e^-. \qquad [5]$$

The potential profiles of the CNTs/S cathode, Zn anode, and hybrid cell are exhibited in Fig. 4*G*, which shows that the output voltage of this hybrid cell can be increased to 0.75 V and it can afford an energy density of 930.9 Wh kg^{-1}_{sulfur}. Based on a high output voltage and energy density, a plastic pouch–type battery pack was fabricated and lights up the light-emitting diode group with the form of "PbS" pattern (Fig. 4*H*). In general, these excellent electrochemical properties of the Pb-S battery and the powerful hybrid cell confirm the substantial research value of Pb-S chemistry in energy storage.

Conclusion

In summary, in this study we report a reliable Pb-S battery based on a dual conversion reaction mechanism. Unlike the stripping/plating–type counter electrode of a traditional metal-sulfur battery, the conversion-type counter electrode gives the aqueous Pb-S battery the advantage of a dendrite-free nature. Furthermore, the Pb-S battery is endowed with a shuttling-free nature due to the inherent insolubility of PbS. Benefiting from these two advantages, the Pb-S battery exhibited excellent electrochemical properties with a reversible capacity of 960 mAh g^{-1}_{sulfur} after 400 cycles. Notably, we also adopted a general strategy to increase the output voltage of the Pb-S battery by using a Zn anode, which was constructed with a

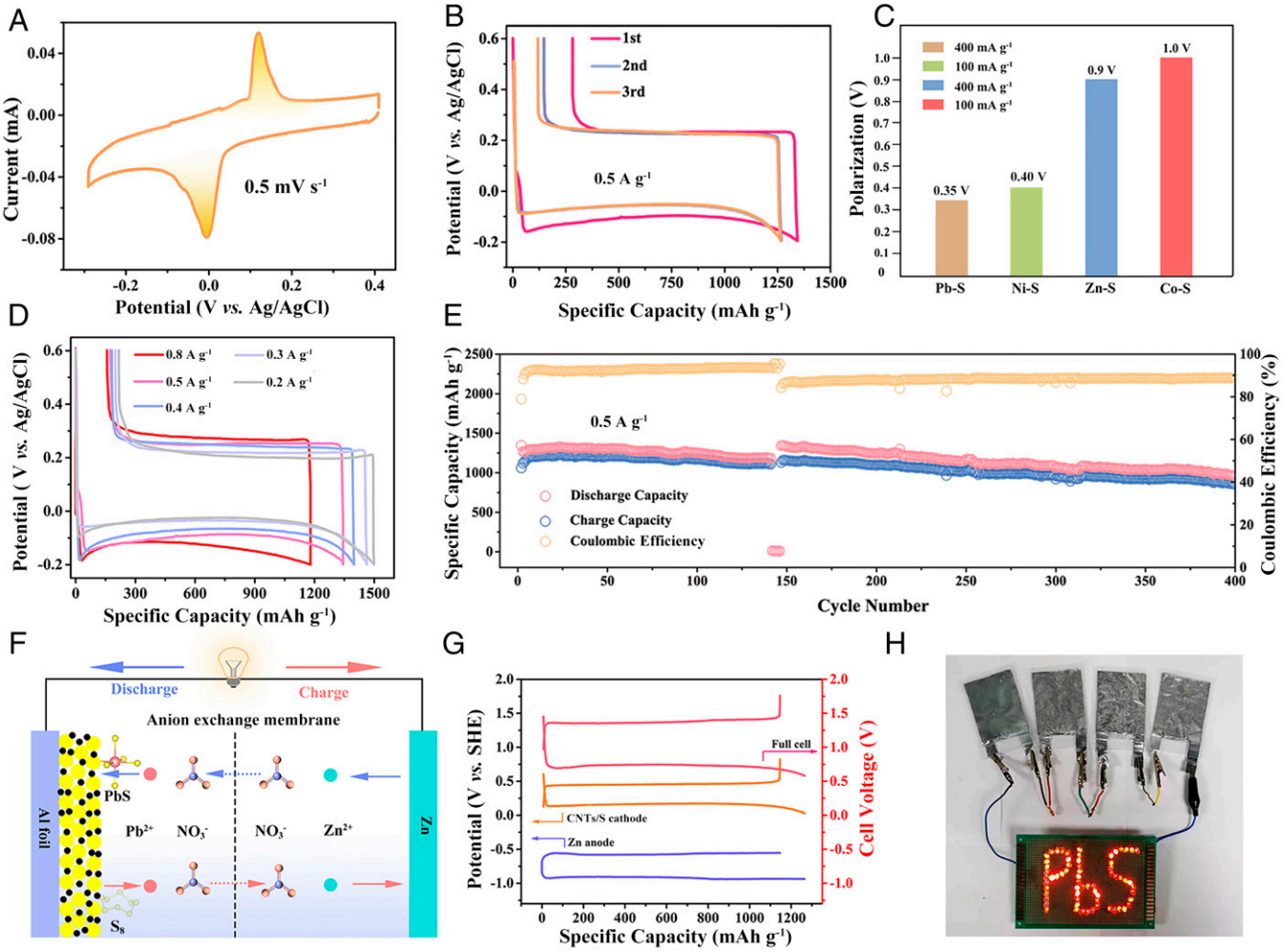

Fig. 4. Electrochemical performance of the aqueous Pb-S battery. (*A*) The first CV curve measured at a scan rate of 0.5 mV s^{-1}. (*B*) The first three GCD curves collected at 0.5 A g^{-1} from −0.2 to 0.6 V versus Ag/AgCl. (*C*) A histogram of the extent of polarization for different M-S batteries. (*D*) Rate performance of the Pb-S battery. (*E*) Long-term cyclic stability of the Pb-S battery. (*F*) Schematic of the working mechanism of the S|$Pb(NO_3)_2$||$Zn(NO_3)_2$|Zn hybrid cell. (*G*) The GCD potential profiles of the CNTs/S cathode, Zn anode, and corresponding hybrid cell. (*H*) A fabricated plastic pouch–type battery pack powered by four hybrid cells. SHE, standard hydrogen electrode.

S|$Pb(NO_3)_2$||$Zn(NO_3)_2$|Zn hybrid cell. Of course, the residual PbO_2 on the anode surface in the charge state is a major factor affecting the performance of the Pb-S battery. In the future, the optimization of the Pb-S system can be carried out around the surface modification of the anode, such as a coating of conductive polymers and introduction of functional groups. In general, our work not only expands the application of metal-sulfur chemistry in energy storage but also provides a guideline for the future development of metal-sulfur batteries.

Materials and Methods

Preparation of the Sulfur Composite. CNTs/S composites were prepared by a facile melt-diffusion method. In a typical synthesis of sulfur composite, 0.6 g sulfur was first ground with 0.4 g CNTs for 20 min. Then, the composite was collected and sealed into an autoclave and heated at 155 °C for 10 h.

Materials Characterization. Powder XRD patterns were collected from 10° to 80° using a Bruker D-8 Advance X-ray diffractometer (Cu Kα radiation, 30 kV and 10 mA) at a scanning rate of 10° min^{-1}. Morphology information was investigated by SEM (Hitachi SU-70) and TEM (JOEL 2100F). Brunauer–Emmett–Teller surface area was measured by an ASAP 2460 instrument by nitrogen adsorption at 77 K. Thermogravimetric analysis was performed on a TG/DTA7300 (Seiko Inc.)

Electrochemical Measurements. The working electrodes were fabricated by smearing a mixture of sulfur composite (80 wt %), acetylene black (10 wt %), and polytetrafluoroethylene (10 wt %) on carbon paper current collector and dried in air at 50 °C. The mass loading was about 4.0 mg cm^{-2}. The electrochemical property of the S/PbS redox couple was evaluated in standard three-electrode cells that consisted of a working electrode, carbon paper counter electrode, and 0.5 mol L^{-1} $Pb(NO_3)_2$ electrolyte. The CV curves were conducted on a Bio-Logic VSP electrochemical workstation. GCD performance was tested by a Land battery tester (LANHE CT2001C).

Data Availability. All study data are included in the article and/or *SI Appendix*.

ACKNOWLEDGMENTS. This work was sponsored by NSAF Joint Fund (Grant U1830106), National Natural Science Foundation of China (Grant U1632114), Science and Technology Innovation 2025 Major Program of Ningbo (Grant 2018B10061), and K.C. Wong Magna Fund in Ningbo University.

1. P. G. Bruce, S. A. Freunberger, L. J. Hardwick, J. M. Tarascon, Li-O_2 and Li-S batteries with high energy storage. *Nat. Mater.* **11**, 19–29 (2011).
2. S. S. Jeong *et al.*, Electrochemical properties of lithium sulfur cells using PEO polymer electrolytes prepared under three different mixing conditions. *J. Power Sources* **174**, 745–750 (2007).
3. J. Wang *et al.*, Sulfur composite cathode materials for rechargeable lithium batteries. *Adv. Funct. Mater.* **13**, 487–492 (2003).
4. X. Ji, K. T. Lee, L. F. Nazar, A highly ordered nanostructured carbon-sulphur cathode for lithium-sulphur batteries. *Nat. Mater.* **8**, 500–506 (2009).

5. L. Jiao *et al.*, Capture and catalytic conversion of polysulfides by in situ built TiO_2-MXene heterostructures for lithium-sulfur batteries. *Adv. Energy Mater.* **9**, 1900219 (2019).
6. X. K. Zhang *et al.*, Copper hexacyanoferrate as ultra-high rate host for aqueous ammonium ion storage. *Chem. Eng. J.* **421**, 127767 (2021).
7. C. Xu *et al.*, Prussian blue analogues in aqueous batteries and desalination batteries. *Nano-Micro Lett.* **13**, 166 (2021).
8. J. Li *et al.*, Insights into host materials for aqueous proton batteries: Structure, mechanism and prospect. *Nano Energy* **89**, 106400 (2021).
9. E. Peled, Y. Sternberg, A. Gorenshtein, Y. Lavi, Lithium-sulfur battery: Evaluation of dioxolane-based electrolytes. *J. Electrochem. Soc.* **136**, 1621 (1989).
10. J. Wang *et al.*, Sulfur-mesoporous carbon composites in conjunction with a novel ionic liquid electrolyte for lithium rechargeable batteries. *Carbon* **46**, 229–235 (2008).
11. X. Chen, T. Z. Hou, K. A. Persson, Q. Zhang, Combining theory and experiment in lithium-sulfur batteries: Current progress and future perspectives. *Mater. Today* **22**, 142–158 (2019).
12. Z. W. Yang *et al.*, Thermodynamic analysis and perspective of aqueous metal-sulfur batteries. *Mater. Today* **49**, 184–200 (2021).
13. X. Wu *et al.*, A four-electron sulfur electrode hosting Cu^{2+}/Cu^{+} redox charge carrier. *Angew. Chem. Int. Ed. Engl.* **58**, 12640–12645 (2019).
14. Z. W. Yang *et al.*, Laser-induced graphene assisting self-conversion reaction for sulfur-free aqueous Cu-S battery. *Adv. Funct. Mater.* **31**, 202103893 (2021).
15. X. Y. Wu *et al.*, Rechargeable iron-sulfur battery without polysulfide shuttling. *Adv. Energy Mater.* **9**, 1902422 (2019).
16. W. Li, K. Wang, K. Jiang, A low cost aqueous Zn-S battery realizing ultrahigh energy density. *Adv. Sci. (Weinh.)* **7**, 2000761 (2020).
17. Y. Zhao *et al.*, Initiating a reversible aqueous Zn/sulfur battery through a "liquid film". *Adv. Mater.* **32**, e2003070 (2020).
18. M. M. Gross, A. Manthiram, Rechargeable zinc-aqueous polysulfide battery with a mediator-ion solid electrolyte. *ACS Appl. Mater. Interfaces* **10**, 10612–10617 (2018).
19. N. Li *et al.*, An aqueous dissolved polysulfide cathode for lithium-sulfur batteries. *Energy Environ. Sci.* **7**, 3307–3312 (2014).
20. R. D. Cakan, M. Morcrette, J. B. Lerichebc, J. M. Tarascon, An aqueous electrolyte rechargeable Li-ion/polysulfide battery. *J. Mater. Chem. A Mater. Energy Sustain.* **2**, 9025–9029 (2014).
21. A. Eftekhari, High-energy aqueous lithium batteries. *Adv. Energy Mater.* **8**, 1801156 (2018).
22. L. Suo *et al.*, "Water-in-salt" electrolyte enables high-voltage aqueous lithium-ion chemistries. *Science* **350**, 938–943 (2015).
23. T. T. Liang, R. L. Hou, Q. Y. Dou, H. Z. Zhang, X. B. Yan, The applications of water-in-salt electrolytes in electrochemical energy storage devices. *Adv. Funct. Mater.* **31**, 2006749 (2020).
24. J. Xie, Z. Liang, Y. C. Lu, Molecular crowding electrolytes for high-voltage aqueous batteries. *Nat. Mater.* **19**, 1006–1011 (2020).
25. D. Chao *et al.*, Atomic engineering catalyzed MnO_2 electrolysis kinetics for a hybrid aqueous battery with high power and energy density. *Adv. Mater.* **32**, e2001894 (2020).
26. D. L. Chao, S. Z. Qiao, Toward high-voltage aqueous batteries: Super-or low-concentrated electrolyte? *Joule* **4**, 1846–1851 (2020).
27. D. Chao *et al.*, Roadmap for advanced aqueous batteries: From design of materials to applications. *Sci. Adv.* **6**, eaba4098 (2020).
28. O. Borodin, J. L. Self, K. A. Persson, C. S. Wang, K. Xu, Uncharted waters: Super-concentrated electrolytes. *Joule* **4**, 69–100 (2020).
29. M. G. Plaza, D. Jiménez, J. Carrasco, J. Martínez, A Ni-Cd battery model considering state of charge and hysteresis effects. *J. Power Sources* **275**, 595–604 (2015).
30. Y. Zeng *et al.*, Engineering high reversibility and fast kinetics of Bi nanoflakes by surface modulation for ultrastable nickel-bismuth batteries. *Chem. Sci. (Camb.)* **10**, 3602–3607 (2019).
31. Y. Zeng *et al.*, Flexible ultrafast aqueous rechargeable Ni//Bi battery based on highly durable single-crystalline bismuth nanostructured anode. *Adv. Mater.* **28**, 9188–9195 (2016).
32. H. Wang *et al.*, An ultrafast nickel-iron battery from strongly coupled inorganic nanoparticle/nanocarbon hybrid materials. *Nat. Commun.* **3**, 917 (2012).
33. C. Guan *et al.*, High-performance flexible solid-state Ni/Fe battery consisting of metal oxides coated carbon cloth/carbon nanofiber electrodes. *Adv. Energy Mater.* **6**, 1601034 (2016).